

Original Research

MRI and Histological Analysis of Beta-Amyloid Plaques in Both Human Alzheimer's Disease and APP/PS1 Transgenic Mice

Mark D. Meadowcroft, BS,^{1,2} James R. Connor, PhD,³ Michael B. Smith, PhD,¹ and Qing X. Yang, PhD^{1,3*}

Purpose: To investigate the relationship between MR image contrast associated with beta-amyloid (A β) plaques and their histology and compare the histopathological basis of image contrast and the relaxation mechanism associated with A β plaques in human Alzheimer's disease (AD) and transgenic APP/PS1 mouse tissues.

Materials and Methods: With the aid of the previously developed histological coil, T₂^{*}-weighted images and R₂^{*} parametric maps were directly compared with histology stains acquired from the same set of Alzheimer's and APP/PS1 tissue slices.

Results: The electron microscopy and histology images revealed significant differences in plaque morphology and associated iron concentration between AD and transgenic APP/PS1 mice tissue samples. For AD tissues, T₂^{*} contrast of A β -plaques was directly associated with the gradation of iron concentration. Plaques with significantly less iron load in the APP/PS1 animal tissues are equally conspicuous as the human plaques in the MR images.

Conclusion: These data suggest a duality in the relaxation mechanism where both high focal iron concentration and highly compact fibrillar beta-amyloid masses cause rapid proton transverse magnetization decay. For human tissues, the former mechanism is likely the dominant source of R₂^{*} relaxation; for APP/PS1 animals, the latter is likely the major cause of increased transverse proton relaxation rate in A β plaques. The data presented are essential for understanding the histopathological underpinning of MRI measurement associated with A β plaques in humans and animals.

Key Words: beta-amyloid (A β) plaques; MRI microscopy; iron; APP/PS1 mouse

J. Magn. Reson. Imaging 2009;29:997–1007.

© 2009 Wiley-Liss, Inc.

THE FORMATION OF amyloid-beta (A β) plaques is a neuropathological hallmark and a cardinal feature of Alzheimer's disease (AD). APP/PS1 transgenic mouse models that mimic the formation of human A β plaques in the mouse brain are widely used as an animal model for AD investigations. The development of an imaging technology capable of visualizing and quantifying A β plaques in animal models and in the AD brain is critically important for translational, preclinical and clinical research. The ability to delineate A β plaques with MRI has been demonstrated ex vivo with human brain samples (1) and in vivo with the mouse model (2–4). Understanding the histological basis of MRI contrast associated with A β plaques is essential in this endeavor. To achieve this goal, it is necessary to correlate MRI results with histological stains, which has been technologically challenging because of the limitations in co-registration of planar histology tissue samples with MR images. A prior study involving the innovation of a histological coil has addressed this long-standing difficulty (5). The ability to directly image histological samples is possible when using the developed histological radiofrequency (RF) coil design. Consequently, MR images and histology data from the same tissue sample can be directly overlaid and compared without uncertainties of co-registration between the two imaging modalities. The goal of the current study is to use this novel technology to (i) further optimize the method for routine imaging-histology studies, (ii) establish the relationship between MR image contrast associated with A β plaques and their histology, and (iii) compare such relationships in human and transgenic APP/PS1 mouse tissues. Furthermore, to ultimately apply the therapies developed with the animal models to human studies, the A β plaque MR image-pathology relationship must be validated in humans and compared with transgenic animal data. It is hypothesized within the literature that iron found in and around the amyloid plaques is the dominant cause of the hypointensities seen in the MR images. Examination of the relationship

¹Department of Radiology (Center for NMR Research), Pennsylvania State University College of Medicine, Milton S. Hershey Medical Center, Hershey, Pennsylvania.

²Neural and Behavioral Sciences, Pennsylvania State University College of Medicine, Milton S. Hershey Medical Center, Hershey, Pennsylvania.

³Department of Neurosurgery, Pennsylvania State University College of Medicine, Milton S. Hershey Medical Center, Hershey, Pennsylvania.

Contract grant sponsor: NIH; Contract grant number: 5R01EB000459-4; Contract grant number: R01AG027771; Contract grant sponsor: the George M. Leader Foundation; Contract grant sponsor: the Pennsylvania Department of Health.

*Address reprint requests to: Q.X.Y., Department of Radiology (Center for NMR Research), M.S. Hershey Medical Center, 500 University Drive, Hershey, PA 17033. E-mail: qyang@psu.edu

Received October 14, 2008; Accepted January 9, 2009.

DOI 10.1002/jmri.21731

Published online in Wiley InterScience (www.interscience.wiley.com).

between MR contrast due to A β plaque and iron deposition both in human AD and the APP/PS1 model is described. The data suggest that iron load alone does not account for the hypointensities that are observed in the T $_2^*$ -weighted images of the animal pathology. The relationship of plaque morphology and overall globular size with their manifestation in the MR image are described. The method developed in this report can be particularly useful for further validation of the histological basis of MR contrast and the development of animal models for other neurological diseases.

MATERIALS AND METHODS

Human Alzheimer's and Control Brain Samples

Entorhinal cortex brain tissue samples from clinically and histologically determined AD subjects (n = 5) and age-matched controls (n = 4) were donated with consent following institutional guidelines and obtained from both internal and external sources (Harvard Brain Tissue Resource Center, McLean Hospital, Belmont, MA). Analysis of the tissue obtained from the brain bank indicates that there was not a significant difference between the age of the subjects upon bereavement. The post mortem index between the tissue harvesting at time of death and utilization in this study was significantly different between the tissue samples, with a slightly longer time period for controls. Tissue from the entorhinal cortex was fully fixed in 4% paraformaldehyde in pH 7.3 phosphate buffered saline (PBS) after which blocks of tissue were cryogenically protected in graded sucrose solutions then sectioned at 60 μ m on a cryostat. The sections were prepared for magnetic resonance imaging according to previous methods explained below (5).

Transgenic APP/PS1 and Control Mice

Transgenic mice (n = 5) inserted with a chimeric amyloid precursor protein (APP) (APP^{Swe695}) and a mutant human presenilin 1 (A246E variant), developed by Borchelt et al (6,7), were obtained commercially from The Jackson Laboratory (strain type B6C3-Tg(APP695)3Dbo Tg(PSEN1)5Dbo/J). Animals were kept in the animal facility under veterinary care with normal feeding, environmental, and handling conditions. Age-matched cage mate C57BL/6 mice (n = 3) were used as a control group. Upon aging naturally until 24 months, animals were killed by means of an intraperitoneal injection of sodium pentobarbital (Nembutal, 200 mg/kg) and were transcardially perfused with cold Lactated Ringer's solution (pH 7.4) followed by buffered 4% paraformaldehyde in PBS. Whole brain tissue was harvested, fixed in pH 7.3 buffered 4% paraformaldehyde, placed in graded sucrose solutions for cryoprotection, then sections were cut at 60 μ m and prepared for MR micro-imaging using the protocol below.

Histological Slice MRI Scanning Protocols

Histological MRI was accomplished on a 7.0T magnet (Bruker BioSpin MRI GmbH, Ettlingen, Germany) with

the histological coil (5). Sixty-micrometer tissue samples were floated in PBS for 30 min to allow any residual formalin and sucrose in the tissue to leach out and then encased between the two coverslips. The sample was then placed into the histological RF coil and tuned/matched to 300.48 MHz for micro-MR imaging. For T $_2^*$ imaging, multi-gradient-echo (MGE) images were acquired in 6 hours 32 min with a repetition time (TR) = 718, echo time (TE) = 6.48, flip angle (FA) = 30°, 8 echoes with 9-ms echo spacing, 64 averages, field of view (FOV) = 23 mm \times 23 mm, and a matrix of 512 \times 512 resulting in a final in-plane resolution of 45 μ m \times 45 μ m.

Iron and Amyloid Staining

After histological MR imaging, the 60 μ m tissue sections were free floated and rinsed in deionized water (dH $_2$ O) for 15 min. Tissue sections were co-stained for both iron and beta-amyloid with a Perl's Prussian Blue stain followed by an aqueous Thioflavin-S stain. The sections were placed in equal volumes of freshly prepared 4% potassium ferrocyanide (#P236, Fisher Scientific, Waltham, MA) and 4% hydrochloric acid (final combined concentrations 2% for each) for 30 min under gentle rocking followed by two rinses in dH $_2$ O. Intensification of the iron stain was performed with 5 min of 3,3'-diaminobenzidine tetrahydrochloride (DAB) staining (#D5637, Sigma, St. Louis, MO; 10 mg dissolved in 15 mL of PBS with 16 μ L of 30% H $_2$ O $_2$) followed by two 5-min rinses in dH $_2$ O. Tissue samples were then free floated in 20 mL of 1% Thioflavin-S (#T1892, Sigma, St. Louis, MO) aqueous solution for 5 min, followed by differentiation in 70% ethanol for 5 min and two 5-min washes in dH $_2$ O. Sections were mounted on histological slides with FluorSave Aqueous mounting media (#345789, Calbiochem, San Diego, CA). To test for the possibility of confounding interactions between the two staining methods during co-staining, each was tested on separate tissue samples to determine their individual efficacy and compared with the co-stained sections. A modified Perl's stain further tested the transgenic animal tissue for minute amounts of iron within the amyloid masses. The stain was adapted and modified from LeVine (8,9) and employs the usage of proteinase K and detergents to break down the periphery of the plaques forming openings in the highly hydrophobic amyloid plaques. This allows the aqueous Perl's stain to infiltrate into the amyloid mass and is sensitive enough to detect trace amounts of iron in the A β plaques.

Microscopy

High resolution microscopy of the tissue sections was performed using a Nikon OptiPhot microscope and Nikon Digital Sight camera using NIS-Elements software. Brightfield microscopy under the visible light spectra was used to view iron stains. A fluorescein isothiocyanate fluorescence cube at 430-nm excitation and 550-nm emission was used to visualize Thioflavin-S positive A β deposits. Whole tissue image mosaics were created with the \times 40 magnification bright field and fluorescent images using the Photomerge option in

Adobe Photoshop CS (Adobe Systems Incorporated, San Jose, CA). For transmission electron microscopy (TEM), samples were prepared by cutting tissue sections at 60 μm and staining them with Thioflavin-S to elucidate A β plaque location. Known regions of A β plaque distribution approximately 1 mm \times 1 mm were micro-dissected from the sections and processed for electron microscopy following traditional methods.

MRI and Histology Postprocessing

Postprocessing was performed using in-house software developed with the interactive data language (IDL) 6.1 framework (Research Systems Inc., ITT Industries, Boulder, CO). The program allows for the creation of T_2^* parameter maps from MGE data with a linear regression method. Plaque regions of interest (ROIs) were selected by averaging the relaxation of three pixels of interest within each measured plaque. This allowed for the evaluation of relaxation measurements from individual plaques in both human AD and APP/PS1 tissue. ROIs for nonplaque regions were selected in regions known to be devoid of A β plaques according to the Thioflavin-S staining. For co-registration to the staining methods, T_2^* weighted images were generated by the summation of the amplitude images from all of the echoes. Histology and MRI images were imported into Image J (National Institutes of Health, Bethesda, MD) to measure A β plaque diameter. Freehand boundaries were drawn around the plaques and the average pixel length of the major and minor axes from the resulting ellipsoid were used to estimate overall diameter. A micrometer slide was viewed at different magnifications to obtain precise measurements of the pixel to micrometer dimensions for plaque diameter calculation.

RESULTS

Figure 1 shows a T_2^* weighted MR image and histological images co-stained with thioflavin-S for A β plaques and a traditional Perl's stain for ferric iron (Fe^{+3}) within the same tissue section from the entorhinal cortex of an AD subject. The image scales of the MR scan and stain mosaic images for A β and iron are the same for ease of comparison. For detailed evaluation, $\times 40$ magnification images of four selected regions outlined with red boxes are shown on both sides of the corresponding main images. The T_2^* -weighted images of human Alzheimer's samples show a loss of signal in focal regions that co-registers remarkably well to the histological iron stain. Many hypointense spots can clearly be observed in the gray matter in the MR image in Figure 1a. As seen in the magnification of the thioflavin-S stain images (Fig. 1b), those hypointensities observed in the MR images correspond to either punctate green fluorescent Thioflavin-S positive A β -plaques (red arrows) or dark brown patches indicating regions of high focal iron. Focal regions of high iron that are not associated with A β plaques can be attributed to locations high in iron such as capillary vessels, hemosiderin (degraded ferritin) or regions of iron oxide (magnetite, hematite or wüstite) deposition (blue arrows) (10, 11). Co-staining of A β with Thioflavin-S and iron with a Perl's stain allows

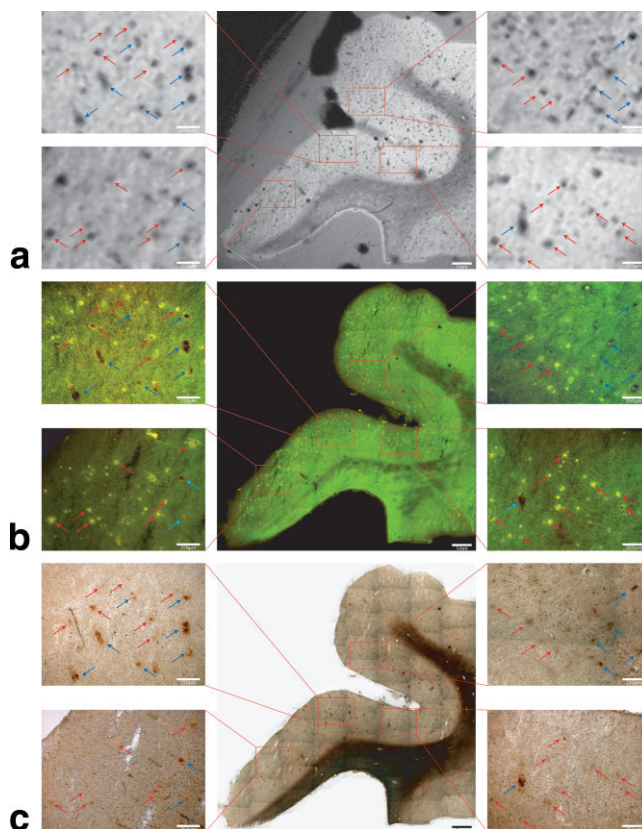


Figure 1. T_2^* weighted MR image (a) and histological images of Thioflavin-S stain for beta-amyloid plaques (b) and Perl's iron stain (c) of the same tissue section from the entorhinal cortex of an Alzheimer's disease subject. For detailed comparisons, images with $\times 40$ magnification of four selected regions outlined with red boxes are shown on both sides of the corresponding main images. A large amount of hypointense spots can be seen clearly in the gray matter in the MR image in a. As seen in b in the Thioflavin-S stain images, these hypointensities are shown either as bright green indicating A β plaques (red arrows) or dark brown indicating small blood vessels (blue arrows). The Perl's stain of the brain tissue in c demonstrates focal high iron concentration in both A β plaques and blood vessels. For the former, a higher iron deposition in A β has been previous demonstrated. For the latter, the elevated iron is likely associated with residual blood, ferritin/hemosiderin or magnetite. As seen in c, select hypointensities in the MR that are due to beta-amyloid plaques are seen with red arrows while signal dropout due to other focal iron regions are highlighted with blue arrows in the four concurrent image magnifications. The figure illustrates that hypointensities seen in the T_2^* weighted image correlate to plaque location and focal iron concentrations. Iron deposition is present in the beta-amyloid plaques that are viewable in the MR image sets. Scale bars = 250 μm and 1 mm for the whole images.

the direct comparison of ferric iron concentration in and around the beta-amyloid plaques (Fig. 1c). The Perl's stain of the tissue section demonstrate focal high iron concentration associated with A β plaques in exceptional detail. Many of the A β plaques seen in the magnified images appear to have a dark core in their centers which are loaded with a higher concentration of iron, as indicated in the Perl's stain. This set of images reveals an unprecedented close relationship with MRI contrast

between A β plaques and brain tissue iron deposition. The minimal AD plaque size diameter that can be resolved with the T $_2^*$ -weighted sequence is 38 μ m, demonstrable with the 250 μ m scale bars in the Figure 1 magnifications. Smaller human AD plaques that do not visibly contain large amounts of iron are not as discernable on the MR images. The high iron distribution within the white matter tracks of the human tissue is consistent with iron found in oligodendrocyte cells making up the myelin sheaths (12). With the histological coil, the relationship between T $_2^*$ image contrast associated with A β plaques and their association with iron deposition are demonstrated unambiguously. The presence of higher iron deposition in the A β plaques is a contributing factor to T $_2^*$ image contrast generation. Regions of gray matter that exhibit high iron content are clearly visible on the MR image with varying degrees of signal dropout differing in size based on the amount of iron present at that location. MR image and histology from a normal brain tissue are shown in Figure 2 and demonstrate a complete absence of A β plaques. The Perl's stained images of the human control tissue sections demonstrate the known patterns of normal iron staining in regions associated with high iron concentration. Iron stains of the human control tissue (Fig. 2c) show the expected high diffuse iron in the white matter tracks due to the high iron concentration within the oligodendrocyte cells (13). This known phenomena can be seen with all histological iron stains and in MR images as a signal dropout. Comparison of white matter iron staining between human AD and control samples shows similar iron deposition illustrating negligible iron loss due to formalin leaching. Fluorescent microscopy shows a lack of Thioflavin-S positive A β staining, while nonspecific background fluorescence is present. Having neither A β plaques nor high focal iron regions, MR images of human control tissue (Fig. 2a) exhibit a lack of hypointensities in gray matter except those caused by the highlighted focal iron regions (blue arrows in Fig. 2) and coil noise. Small hypointensities that are seen in Figure 2 are related to inhomogeneities within the copper foil used in the RF coil, small micro-pockets of air causing artifacts, or small regions of focal iron.

The corresponding images from APP/PS1 and age-matched C57BL/6 control mice tissue sections are shown in Figures 3 and 4, respectively. The image scales of the animal MR images and histology mosaics for iron and A β plaques are the same as in the human data for ease of comparison. The widespread dark spots (red arrows) seen in the human tissue are also shown conspicuously in the T $_2^*$ image of the transgenic animal tissue within the piriform cortex (Fig. 3a). Thioflavin-S staining (Fig. 3b) confirms that these dark spots are A β plaques within the APP/PS1 animal brain. MR imaging of mouse control tissue (Fig. 4a) shows no evidence of focal hypointense regions in the neocortex. The iron stain of the control mouse tissue in Figure 4c shows that there are no visible focal iron regions in the neocortex or other gray matter regions. Thioflavin-S staining does not indicate any positive amyloid staining for plaques in mouse control sections apart from the expected nonspecific background staining. Regions that

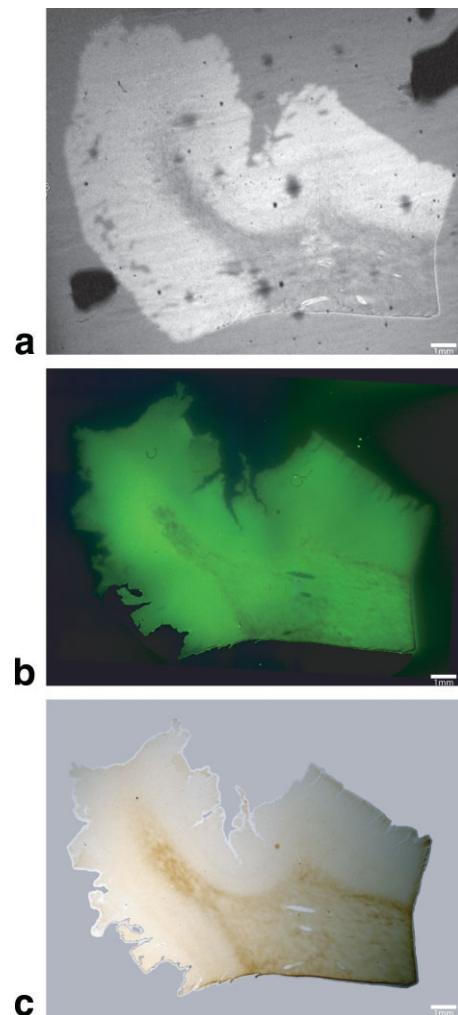


Figure 2. MRI, thioflavin-S, and iron stains in human control subjects. An MGE T $_2^*$ weighted image (a), thioflavin-S (b), and Perl's iron stain (c) of the same 60 μ m thick tissue section from the entorhinal cortex of an Alzheimer's disease subject. The T $_2^*$ image shows hypointensities that are due to micro pockets of air or coil inhomogeneities. The thioflavin-S stain illustrates a lack of beta-amyloid plaques in the human control subjects. Perl's staining shows high iron in white matter tracks due to oligodendrocytes and one focal iron region in gray matter in the Perl's stain image and can be seen as a signal drop in the MR image. Scale bars = 1 mm in all images.

are known to be high in iron, such as the substantia nigra and caudate/putamen, stain dark as expected (Fig. 3c) (14). The plaque distribution is consistent with previous studies using the APP/PS1 transgenic mouse line (4,15–17), while plaques are not present in the C57BL/6 control animal tissue. Measurements of the plaques within the APP/PS1 model indicate that MR microscopy observable plaques have a minimum diameter of approximately 40 μ m, which is very similar to the human AD samples. Smaller plaques are also visible with Thioflavin-S staining throughout the neocortex (barrel fields, somatosensory, motor, and granular cortices), hippocampus, thalamic region, caudate, and putamen of the animal brain but are not visible in the MR images. The most prominent difference between the

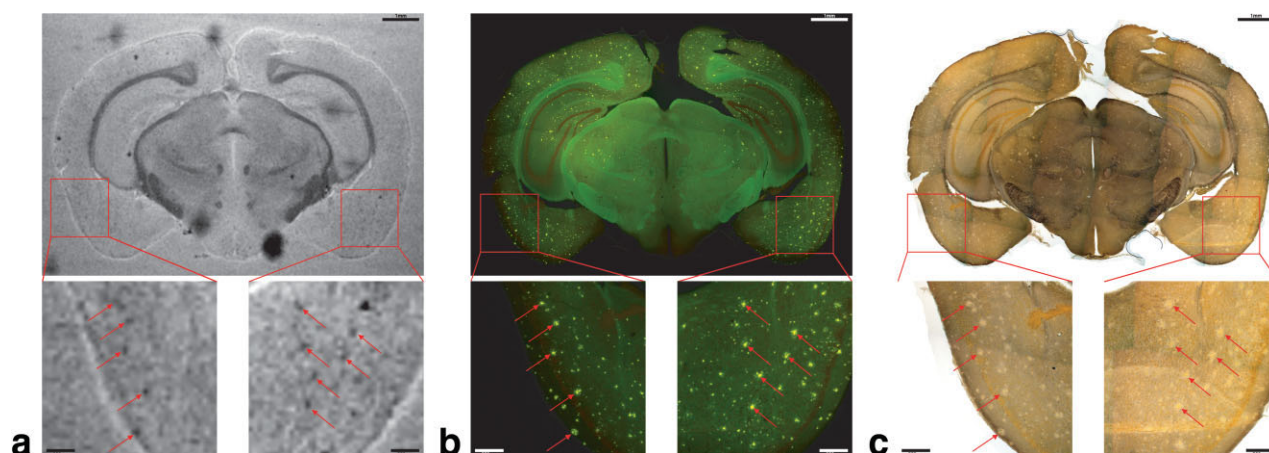


Figure 3. Co-registration of MRIs (a), beta-amyloid (b), and iron stains (c) in the APP/PS1 mouse model. **a:** An MGE T_2^* weighted image of a $60\mu\text{m}$ slice from a APP/PS1 mouse brain at approximately -2.92 mm Bregma. Final in-plane image resolution was $45\mu\text{m} \times 45\mu\text{m}$. Image magnifications ($\times 40$) of the selected regions of interest within the left and right piriform cortex are seen below. Hypointensities are noted by red arrows. **b:** Thioflavin-S fluorescent mosaic image of the same tissue section in 1a. Beta-amyloid staining is evident and can be seen as the bright green positions. The same regions as in 1a have been magnified with the arrows pointing toward the plaques responsible for the T_2^* weighted hypointensities. **c:** Perl's iron stain with the same magnifications and regions of interest arrows as in 1a and 2a. The figure illustrates that the hypointensities seen in the T_2^* weighted image are in the same region as large beta-amyloid plaques approximately $50\text{--}60\mu\text{m}$ in diameter. Iron deposition is not present at the plaque locations, as they seem to be regions of low iron concentration compared with the surrounding gray matter tissue. Scales bars = $250\mu\text{m}$ and 1mm for the whole image.

human AD (Fig. 1b,c) and APP/PS1 mouse tissues (Fig. 3b,c) involves the focal iron concentration found in the vicinity of the $A\beta$ plaques. Large amounts of focal iron are found within and around the Thioflavin-S positive amyloid plaques in the human AD tissue, while very little is seen in the APP/PS1 tissue. In the magnified images, the plaques indicated by the red arrows in Figure 3b coincide with the white patches in Figure 3c, suggesting lower iron content in these areas. This observation seems to be in opposition to what has been demonstrated in the human AD tissues. No dark iron-cored plaques were observed in the transgenic animal histological images compared with the human AD sections. This is also at seen at higher magnification, as illustrated at $\times 100$ in Figure 5. $A\beta$ plaques in human AD tissue appear to be small cored plaques surrounded by large diffuse coronas while the plaques in the APP/PS1 mouse tissue exhibit larger dense cores made of compact fibrillar $A\beta$ protein deposition with a smaller diffuse corona region. The Alzheimer's tissue samples demonstrate the localization of iron (Fig. 5b) within the amyloid plaque mass (Fig. 5a). Transgenic animal tissue shows a high concentration of large amyloid deposits while co-staining with the traditional Perl's ferric iron stain does not show regions of high iron within these plaques. Staining capillaries high in iron serves as a positive control for the effectiveness of the traditional Perl's stain for detecting iron, indicated by arrows in Figure 5c,d. Minor digestion of the $A\beta$ plaque periphery in the APP/PS1 tissue and staining with the modified Perl's technique are shown in Figure 5e,f. There is visible evidence of trace amounts of iron in the transgenic animal plaques that was not stainable with the traditional method. The iron load within the APP/PS1 plaques is very minute compared with the human AD tissue. Staining the human AD tissue (not shown) with

the modified Perl's technique rendered the samples completely brown, which is indicative of iron throughout the tissue samples. There is a possibility that the protein digestion also exposed the ferrihydrite and magnetite core of the ferritin complexes in these samples allowing the Prussian blue reaction to occur throughout the sample (18). This result rendered the microscopic detection of focal iron around Thioflavin-S plaques impractical for human AD sections stained in this manner. The iron stain of both APP/PS1 and control animal tissue does show appropriate tissue iron distribution as evident in the known high iron brain structures such as the substantia nigra, striatum, and white matter tracks (19). High magnification $\times 6000$ and $\times 46,000$ transmission electron microscopy images of amyloid plaques from both APP/PS1 and human AD can be seen in Figure 6a,b, respectively. Each plaque in Figure 6a,b is similar in size, approximately $10\mu\text{m}$ in diameter. The $\times 6000$ images include the whole plaque within the viewing plane and illustrate that $A\beta$ plaques in the APP/PS1 model have a denser overall structure than the plaques found in human AD. Higher $\times 46,000$ magnification of the outlined regions shows fibrillar $A\beta$ strands in both AD and APP/PS1 tissue and further demonstrates the difference in density between AD and APP/PS1 plaques.

For quantitative MRI studies, Figure 7a graphically shows average relaxation values for regions of interest that included and excluded $A\beta$ plaques within the AD sample and regions within the gray matter of the control sample. Average R_2^* measurements for the AD tissue samples were 30.33 ± 3.86 (1/s) in regions with plaques and 16.10 ± 2.92 (1/s) in regions without plaques. Control tissue R_2^* relaxation rate was 14.54 ± 2.01 (1/s). R_2^* relaxation rates for the regions with plaques were significantly higher ($P < 0.0001$) than

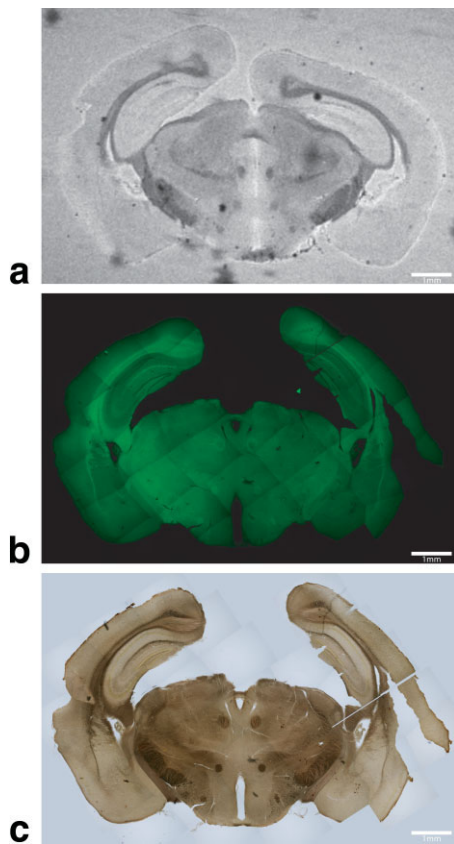


Figure 4. MRI, thioflavin-S, and iron stains from a control C57BL/6 mouse. An MGE T_2^* weighted image (a), thioflavin-S (b), and Perl's iron stain (c) of same 60- μm -thick section of tissue from a C57BL/6 control mouse at approximately -2.80 mm Bregma. The T_2^* weighted image shows hypointensities and iron staining at regions of known high iron concentration such as the substantia nigra, white matter tracks and the caudate/putamen. Thioflavin-S staining reveals only nonspecific background staining with no beta-amyloid plaques in the control animals. There are no MR hypointensities that are associated with positive thioflavin-S staining. Scale bars = 1 mm in all images.

both the controls and regions without plaques. Relaxation measurements in regions without plaques were not significantly different from control tissue. Average relaxation values for gray matter regions in the APP/PS1 mice that included or excluded A β plaques and control animals are seen in Figure 7b. Average R_2^* measurements for APP/PS1 were 24.84 ± 3.67 (1/s) in regions with plaques and 18.40 ± 1.47 (1/s) in regions without plaques. C57BL/6 controls had an average R_2^* relaxation of 18.75 ± 1.03 (1/s). Regions with plaques in the APP/PS1 animals had a significantly higher R_2^* relaxation compared with both control tissue and regions without plaques ($P < 0.0001$). Measurements of R_2^* relaxation were not significantly different between regions of interest in the transgenic animal devoid of plaques and control mouse tissue.

DISCUSSION

Understanding the relationship between beta-amyloid plaque pathology in AD and the associated MRI con-

trast is fundamentally important for MRI study of AD pathology. This work demonstrates the ability to image A β plaques in histology sections of both human AD and amyloid-generating APP/PS1 transgenic mice brains. The histological MR images taken at a field strength of 7.0 Tesla (T) clearly show high resolution details of A β plaques in human and animal samples. Previous MRI studies of A β plaques have been carried out with blocks of human AD brain tissue samples (1). With this approach, accurately matching histological sections of the whole tissue block with the MRI image slice is difficult. Using the histological RF coil, MRI and histological

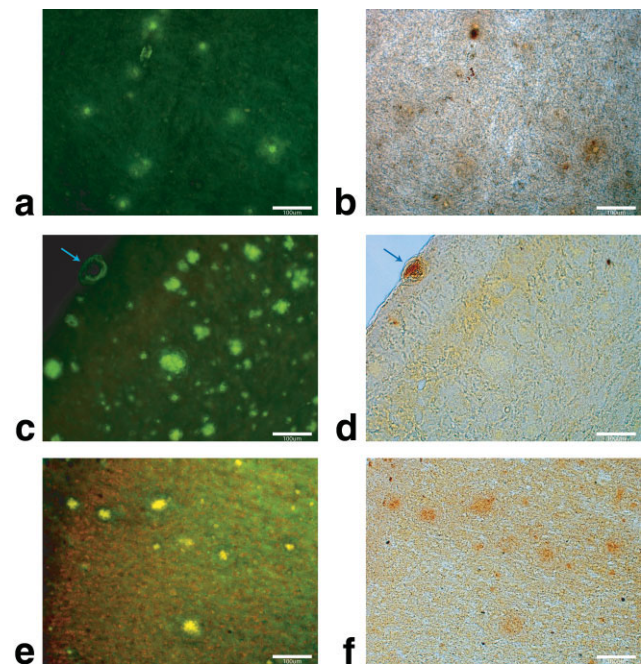


Figure 5. High magnification ($\times 100$) images of beta-amyloid plaques in both human Alzheimer's entorhinal cortex (a,b) and APP/PS1 animals piriform cortex (c-f). The thioflavin-S stain (a) and traditional Perl's stain (b) illustrate a close relationship between beta-amyloid plaques and focal iron deposition in Alzheimer's disease. This relationship between plaques (c) and iron (d) is not clearly seen in the APP/PS1 animals with traditional Perl's staining. The arrows in c and d illustrate iron deposition in a capillary of the APP/PS1 animal demonstrating the positive stain for iron. Staining with a modified Perl's technique (e,f) by means of degradation of the plaques' periphery proteins allows the aqueous stain to penetrate the plaques more readily. There is an indication of minute amounts of iron in the transgenic animal plaques that is not perceivable with the traditional Perl's stain. Differences in plaque morphology between the AD and APP/PS1 animals is evident in images a and c,e. The human AD plaques have a dense core of fibrillar amyloid protein with a halo of amyloid protein around them that is less susceptible to thioflavin-S staining. APP/PS1 A β plaques show a larger and denser thioflavin-S positive core with a smaller halo region around them. The Perl's stains indicate that high concentrations of iron found throughout the human AD plaques is associated with the amyloid protein or within cells such as microglia inside the space the plaque has occupied. Compared with the human AD plaques, the APP/PS1 images show a reduction in focal iron within the plaques that is diffusely found throughout the plaque. Scale bars = 100 μm .

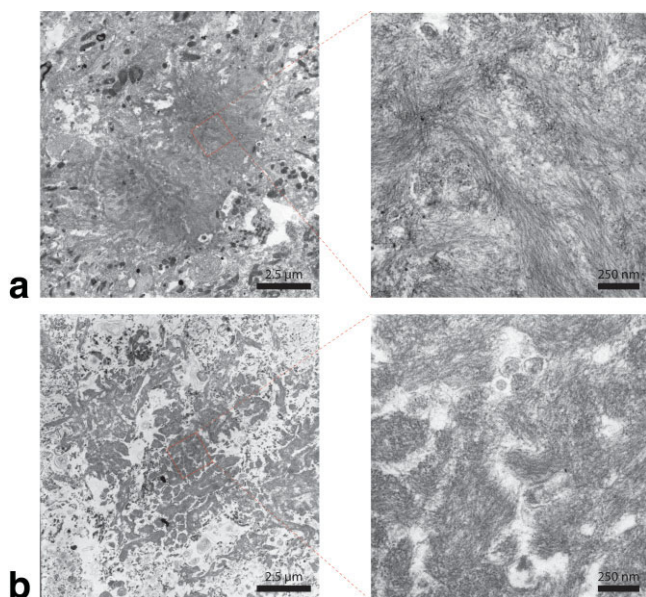


Figure 6. Transmission electron microscope images of plaques in APP/PS1 (a) and human AD (b) tissue. The $\times 6000$ magnification images of the plaques include the whole plaque within the imaging plane. The plaque diameter for both APP/PS1 and AD tissue is approximately the same, at $10\ \mu\text{m}$. The lower magnification image illustrates the denser overall structure of the beta-amyloid plaques in the APP/PS1 compared with the human AD tissue. The human AD plaques have numerous gaps present between the fibril bundles throughout them that are rarely found in the transgenic mouse plaques. The $\times 46,000$ magnification of the outlined regions reveal differences in the fibrillar orientation of the beta-amyloid strands in the APP/PS1 and AD plaques. Magnification of the outlined regions also illustrates the denser nature of the APP/PS1 plaques while the human AD tissue has gaps between amyloid strand clusters. [Color figure can be viewed in the online issue, which is available at www.interscience.wiley.com.]

analyses were performed on the same tissue sample so that tissue pathology and associated MRI contrast changes could be precisely compared. This capability allowed us to establish a one-to-one relationship be-

tween MRI parameters and histology data acquired from human AD and APP/PS1 transgenic mouse tissue samples. Such a relationship is important for the interpretation of MRI findings in the AD brain and its animal models. Additionally, the information acquired with this technology is valuable in the development of potential therapies for AD research and investigations of other pathologies.

The MR imaging of amyloid plaques in transgenic APP/PS1 mice has been pioneered by several groups using both in vivo and ex vivo imaging methodologies (4,15,16). The hypointensities in the MR images of APP/PS1 animal tissue that coincide with the plaques are similar in signal dropout and size compared with MR images of human AD plaques (Figs. 1, 3). The cause for the hypointensities seen in T_2^* and T_2 weighted images of APP/PS1 mice thus has been believed to be caused by high iron accumulation in the plaques (4,15,16). However, when viewing the iron and $A\beta$ stained images in Figures 3 and 5, the iron concentration is significantly reduced in the APP/PS1 $A\beta$ plaques compared with the human AD tissue in Figure 1c, while $A\beta$ -plaques in APP/PS1 and human AD samples are perceptibly the same when viewed with MR images. To confirm that the staining methods did not cause aberrant interactions with one another, independent iron and amyloid stains were performed yielding the same appearance as co-staining procedures. To understand this unexpected result, notice that APP/PS1 plaques in Figures 3b and 5 show an extremely dense nature, which suggested that the current traditional Perl's staining method might not be able to stain the iron inside these plaques. The hydrophobic nature of the plaques coupled with the acidic aqueous-based Perl's stain could prevent the Prussian blue reaction from occurring if the stain cannot infiltrate into the plaque. A modified Perl's stain (8) was tested that uses protein degradation and detergents to break down the outer surface of the plaques to allow better peripheral penetration of the aqueous stain. With the modified stain, the images in Figure 5f indeed exposed minute focal

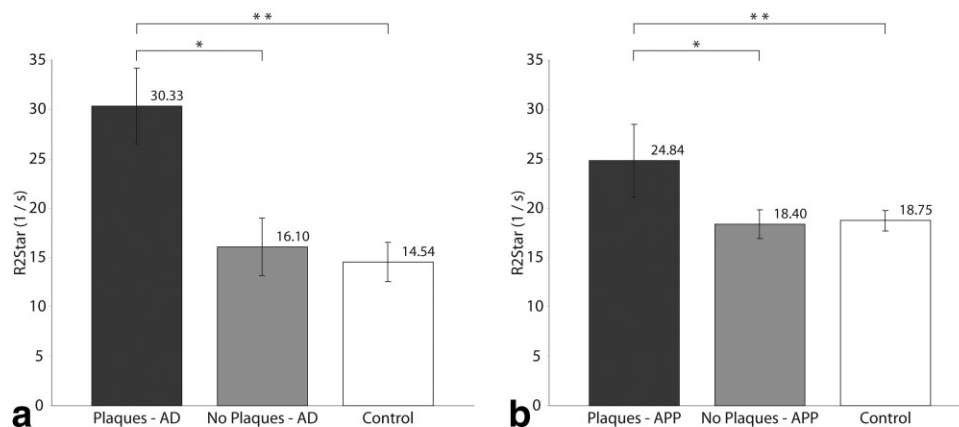


Figure 7. Bar graphs of average R_2^* rates from ROIs with plaques, without plaques and control tissue within human (a) and mouse (b) tissue. The R_2^* relaxation rate of plaque ROIs in the AD tissue is significantly higher than both regions without plaques and control tissue sections. A similar trend is found in mouse data. There is also a higher R_2^* relaxation rate for the plaque ROIs in AD than in the APP/PS1 mouse, hypothesized to be due to higher iron in the AD plaques as shown with the Perl's stain in Figure 5b,d,e.

iron distributions within the APP/PS1 transgenic animal plaques, but much less than that in the human AD plaques. As a control condition, application of the modified stain to human AD tissues resulted in dark brown staining throughout the entire tissue sample (not shown). This could be due to staining of not only the free labile iron pool but additionally iron bound inside ferritin cores that can be stained only when the proteins are digested open with the modified staining procedure. The above observations suggested that iron in the animal plaques is significantly less than that in the human plaques and the plaques in the animals are much denser than those in human samples. Because MR images of the plaques in both human and animals appeared essentially the same, the differing characteristics of the animal plaques raised a fundamental question as to the cause of the MR image contrast associated with the animal plaques.

It is well known that T_2 and T_2^* relaxation and contrast can be altered in a variety of manners. Iron bound within the ferrihydrite-like core of ferritin, hemosiderin, and an assorted number of iron oxide mineral deposits is found in sufficient quantities in the brain to alter MRI contrast (20–24). As a ferromagnetic ion, ferric iron (Fe^{+3}) is known to cause a shortening of T_2 relaxation due to the creation of microscopic magnetic field inhomogeneities that de-phase the signal of water protons in the vicinity (19,25,26). Thus, ferric iron in brain tissue acts as a natural contrast agent causing faster proton T_2 and T_2^* relaxation. There is some evidence to support that small amounts of ferrous iron (Fe^{+2}) is also stained with the Perl's stain reaction (27). The effect of ferrous iron on T_2^* and T_2 relaxation is much less pronounced than that caused by the ferric form (28) (our laboratory's unpublished data). Thus, the signal hypointensities seen in the MR images associated with focal iron regions is likely dominated by the ferric form. One other important factor associated with the MRI appearance of plaques is their size under given experimental conditions (pixel resolution, TE/TR times, etc.). The minimal plaque size viewable in our MR images of the APP/PS1 mice was similar to the AD tissue images, approximately 40 μm and 38 μm , respectively. Thus, due to the similarity in the plaque size for both species, plaque diameter alone does not account for the hypointensities seen in the APP/PS1 data. This is also supported by the fact that human AD plaques of a similar diameter with low observable iron are marginally visible on the MR images, while APP/PS1 plaques with a significantly less iron association are clearly discernable on the MR images. Magnification of the thioflavin-S-positive plaques ($\times 100$ seen in Fig. 5 and $\times 6000$ and $\times 46,000$ in Fig. 6) shows a distinct difference in plaque morphology between AD and APP/PS1 mice. Differences between human AD and the APP/PS1 A β plaques are most noticeable in the TEM magnifications. The human AD plaques consist of fragmented patches with random fibrillar orientation in the amyloid core while the structure of transgenic mouse plaques appears to be a highly packed aggregation of long and oriented fibrils. The decreased density of the amyloid core creates gaps that are prevalent in the human AD plaques while rarely found in the transgenic mouse

plaques. The APP/PS1 mice thioflavin-S data illustrates that, while the plaques are a similar size to those in AD tissue, the plaques have a larger center core of dense compact amyloid. In previous studies, comparison of the structure of the amyloid fibril in the transgenic APP/PS1 model and human AD is subtly different due to posttranslational modifications leading to alterations in the A β molecule (29–31). Plaques found in the APP/PS1 mouse model have a variable distribution of both human and mouse amyloid in the plaques. Diffuse plaques have an intermingled distribution of both human and mouse amyloid, while dense plaques are composed of human amyloid cores surrounded by mouse amyloid (32). Thioflavin-S is known to bind to fibrillar but not to diffuse A β deposits (33,34). The difference in Thioflavin-S staining between human AD and APP/PS1 mice could be due to the different primary fibrillar or diffuse composition of the plaques. Many of the amino acid residue positions within the A β protein are hydrophobic and are sufficient for amyloid fibril formation (35,36). With the additional two hydrophobic amino acids found in the A β_{42} , it aggregates more readily than A β_{40} (37). These views suggest that the hydrophobic regions are at least partially responsible for the fibril formation (38). The morphology of the mouse plaques with their large globular nature and the dense center core seem to be responsible for the T_2^* relaxation associated with these plaques. Unlike smaller proteins, the amyloid mass found in the animal plaques is rigid and fixed in the tissue resulting in a situation where the protein mass would behave similar to a polymer-like solid. This creates several consequences that may affect relaxation in the plaques. First, it sets up an environment where a large amount of available surface area is present inside the plaque mass along the component A β fibrils. Water molecules then become bound to the hydrophilic regions of the fibril axis while repelled by the hydrophobic regions. Water in the immediate vicinity of the hydrophilic regions is bound by means of hydrogen bonding such that it is rotationally or irrotationally bound. Layers of water are affected as they diffuse near the bound water. Cross-relaxation between the protons of bound water and the protein molecules by proton-proton magnetization exchange could lead to a more rapid relaxation of water protons. As such, the relaxation of bound water on the A β fibril chains would act as a relaxation sink for water moving in the surrounding area (39,40). As a result, T_2 relaxation shortening occurs. Second, the magnetic susceptibility differences between the highly compact A β protein mass and surrounding issues could induce static dephasing in addition to that caused by deposited iron. Third, tissue hydration could be also a significant contributing factor for plaque contrast. The dense formation of the animal plaques as indicated in the TEM image limits free water from accessing their core. As shown by histology results, staining iron in the plaques in the APP/PS1 mouse was difficult following standard methodology without protein degradation treatment. These experimental data suggest that access of free water molecules to the animal plaque is very limited. For human samples, the gaps seen between the A β patches (Fig. 6b) would accommodate more free water pools. The trans-

verse relaxation of these water molecules is shortened by the magnetic inhomogeneities caused by ferromagnetic iron in the plaques. Thus, with these observations we would suggest a dual relaxation mechanism for the generation A β plaques T $_2^*$ contrast associated with both the compact fibrillar protein mass and iron deposition. The focal iron concentration could play a dominant role for rapid T $_2^*$ relaxation in human AD plaques while the increased fibrillar density and compacted morphology would be more likely a major factor for T $_2^*$ shortening in the APP/PS1 transgenic plaques. Although the potential relaxation mechanisms in A β plaques discussed above are preliminary and speculative, it is important to realize that alternative relaxation mechanisms must be considered. To thoroughly develop and validate the model of relaxation in A β plaques, more experimental studies are required in future investigations. In addition, caution should be used when comparing ex vivo R $_2^*$ contrast obtained in the fixed tissue samples and extrapolating this to in vivo conditions (5).

The quantitative comparison of the R $_2^*$ maps from different tissue types supports our hypothesis in regard to the relaxation mechanism associated with A β plaques. The mean R $_2^*$ for the selected amyloid plaques in the AD tissues (Fig. 7a) is on average 90% greater than that from the ROIs without plaques and control tissue. Regions in AD gray matter with no A β plaques and in control tissue samples (Fig. 7a) have no statistical difference in relaxation time. However, there is a trend of faster R $_2^*$ relaxation rates in regions without plaques throughout the Alzheimer's tissue compared with control tissue samples. This is indicative of a higher overall iron concentration in the AD neural tissue compared with the control tissue, possibly due to a systemic inability to regulate iron properly within the brain. Iron staining of the tissue samples supports this, which shows an overall increase in high focal iron in the AD tissue samples that is not seen in the control tissue. In the mouse tissue samples (Fig. 7b), the mean R $_2^*$ for the selected amyloid plaques is on average 56% higher than that in the ROIs without plaques and in the control tissue. The mean R $_2^*$ of regions without plaques and of control tissue are nearly identical, indicative of similar tissue fixation across tissue subtypes and consistent preparation of tissue samples. This information alleviates the confounding possibility that separate tissue handling procedures are the source of the observed MR contrast differences. Comparison of R $_2^*$ in ROIs with plaques in both human and APP/PS1 animals tissues reveal that the human plaques have a significantly higher R $_2^*$ value. It is conceivable that human plaques have a duality of relaxation where both high focal iron concentration and fibrillar A β masses cause rapid proton transverse magnetization decay. APP/PS1 plaques exhibiting slower decay due to the reduced concentration of iron is a reasonable explanation for this result. The R $_2^*$ for normal human tissues also appeared to be higher than that of animal tissue. This is consistent with the overall higher iron content in human neural tissue compared with the APP/PS1 animal samples. Iron staining for regions without plaques in the gray matter of APP/PS1 tissue and mouse control tissue samples exhibit similar patterns of iron staining.

These findings generate several important questions regarding the difference between A β plaques found naturally occurring in the human Alzheimer's brain and transgenically introduced into the APP/PS1 animal model. Previous studies have revealed that A β -plaques in APP/PS1 animal show numerous differences from human AD plaques, including plaque morphology and composition (31,41). The difference in morphology and the reduction of iron staining in the plaques raises the question for translating the APP/PS1 model's data to human AD as it is hypothesized that there is a link between A β plaques and elevated iron in the brain tissue as the cause of oxidative stress leading to cellular neurotoxicity (42,43). The relationship of iron to plaque generation is not currently well understood within the literature and is a subject of much investigation. An imbalance in the iron regulatory system and a dysfunctional difference in mineralization of iron within the ferritin core in AD subjects has been previously demonstrated (11,44). It is largely unknown whether the initial generation of the plaque causes the aggregation of iron or if aberrant regulation of extra- or intracellular iron stores cause the formation of the A β protein around it. There is general agreement that the location of A β plaques in human AD brain tissue coincides with focal iron deposits. Iron associated with plaques can accumulate from several potential sources. As a metalloprotein, free iron will bind to A β fibrils and collect within the plaques. Iron from ferritin, and its degradation to hemosiderin, can originate from nearby neurons and microglial cells that have migrated to the A β plaques and can become part of the plaque mass (45-47). Biogenic magnetite found proportionally higher in AD ferritin cores than normal aged human neural tissue is known to accumulate within A β plaques (10,11). While it is unknown precisely how A β plaque aggregation occurs, it is known that metal ions do play a role in A β fibril formation. The conversion of A β 's secondary protein structure to a β -sheet has been shown to occur in the presence of divalent metal ions, including ferrous iron (48). The component fibrils of the A β plaques are known metalloproteins and possess metal chelation regions in their amino-acid sequence (49). The MR and histological images in Figure 1 demonstrate that A β plaques are consistently associated with elevated iron load in and around their vicinity in human AD brain tissue. Research has shown that the colocalization of iron with the human A β plaques is accompanied by endoplasmic reticulum stress induced apoptosis, DNA oxidation and cellular damage in cells adjacent to plaques. Conversely, in regions where A β plaques accumulate alone without iron there is no indication of oxidative stress or apoptosis pathway activation (50). It has been demonstrated that the toxicity of A β is amplified upon the direct interaction of iron ions with the A β peptide, while unbound iron itself has no effect upon toxicity (51). This strongly suggests that A β plaques by themselves are not toxic to cells adjacent to plaques, whereas iron accumulation in and around plaques is essential for neuronal damage. The morphology and associated iron dissimilarity between the human AD and transgenic APP/PS1 plaques raises a question regarding differing amyloidogenesis processes for each

species. In the APP/PS1 mouse model used here, plaques are produced in the brain as early as six months after birth and are believed to continually grow throughout the life span of the animal (52). Current understanding of human amyloidogenesis suggests that plaque generation occurs over years, perhaps decades, and places the plaques into discrete classes based upon the morphology of the plaque and surrounding tissue. It is hypothesized that plaques start out as a seed formation of A β peptide and eventually become much more compact and dense over time (53). The APP/PS1 model generates plaques at a rapid pace and iron staining indicates a reduced amount of iron associated with these plaques compared with AD tissue. It is plausible that the rapid fibrillarization from A β oligomers into compacted fibrillar plaques could lead to less iron deposition within the plaques in the APP/PS1 model.

In summary, imaging of thin slices of tissue samples with the aid of the histological coil allows the one-to-one comparison of tissue pathology as seen in histological stains and different MRI methodologies. With this technique, the relaxation mechanisms for A β plaques in human Alzheimer's disease and the APP/PS1 mouse model were investigated with respect to their morphology and relationship with iron deposition. The histology stains of AD and APP/PS1 tissue samples were directly compared with T $_2^*$ -weighted images and R $_2^*$ parametric maps. The histological iron stains presented here support the hypothesis that iron associated with the A β plaques in the human AD samples plays a major role in generation of MRI T $_2^*$ contrast. Histological data from previous studies using postmortem human AD tissue (14,45,54,55) also support the notion that focal iron load in A β plaques is the dominant cause for faster T $_2$ and T $_2^*$ decay. The electron microscopy and histology data revealed that there are important differences in plaque morphology and associated iron concentration between transgenic APP/PS1 mice and human AD tissue samples. In the Alzheimer's tissue, beta-amyloid plaques with high iron concentration are clearly visible in the T $_2^*$ -weighted images while others of similar size with less focal iron are not as discernable. In the APP/PS1 animal tissue, large plaques are equally observable as human plaques in MR imaging while iron load is significantly less than human plaques. This suggests that there is a degree of difference between the amyloid plaques in the APP/PS1 mouse model and human Alzheimer's, in respect to their morphology and relationship with in vivo iron stores. The increased transverse proton relaxation rate in A β plaques in animals is likely caused mainly by the interactions of water with the highly compacted amyloid fibril mass. The improved resolution of the ex vivo data set allows for the detailed comparison between tissue histology and MR contrast that is not possible with current lower resolution clinically based protocols. The extrapolation of microscopic MR images to in vivo applications is promising in the near future considering the rapid increase in achievable image resolution with the development of higher magnetic fields and the usage of parallel imaging technology (56). The data presented in this report are essential for understanding the histopathological underpinning of

MRI measurement of A β plaques in humans and animal models for both current and future MR applications.

ACKNOWLEDGMENTS

The authors thank Dr. Michael Garwood of the CMRR at the University of Minnesota for his insightful discussion in regard to the transverse relaxation mechanism and Roland Myers of the Electron Microscopy Core Facility for help with the transmission electron microscope data collection. This study was funded by the Pennsylvania Department of Health using Tobacco Settlement Funds.

REFERENCES

1. Benveniste H, Einstein G, Kim KR, Hulette C, Johnson GA. Detection of neuritic plaques in Alzheimer's disease by magnetic resonance microscopy. *Proc Natl Acad Sci U S A* 1999;96:14079-14084.
2. Jack CR Jr, Garwood M, Wengenack TM, et al. In vivo visualization of Alzheimer's amyloid plaques by magnetic resonance imaging in transgenic mice without a contrast agent. *Magn Reson Med* 2004; 52:1263-1271.
3. Jack CR Jr, Marjanska M, Wengenack TM, et al. Magnetic resonance imaging of Alzheimer's pathology in the brains of living transgenic mice: a new tool in Alzheimer's disease research. *Neuroscientist* 2007;13:38-48.
4. Jack CR Jr, Wengenack TM, Reyes DA, et al. In vivo magnetic resonance microimaging of individual amyloid plaques in Alzheimer's transgenic mice. *J Neurosci* 2005;25:10041-10048.
5. Meadowcroft MD, Zhang S, Liu W, et al. Direct magnetic resonance imaging of histological tissue samples at 3.0T. *Magn Reson Med* 2007;57:835-841.
6. Borchelt DR, Davis J, Fischer M, et al. A vector for expressing foreign genes in the brains and hearts of transgenic mice. *Genet Anal* 1996;13:159-163.
7. Borchelt DR, Ratovitski T, van Lare J, et al. Accelerated amyloid deposition in the brains of transgenic mice coexpressing mutant presenilin 1 and amyloid precursor proteins. *Neuron* 1997;19:939-945.
8. LeVine SM. Iron deposits in multiple sclerosis and Alzheimer's disease brains. *Brain Res* 1997;760:298-303.
9. LeVine SM. Oligodendrocytes and myelin sheaths in normal, quaking and shiverer brains are enriched in iron. *J Neurosci Res* 1991; 29:413-419.
10. Collingwood JF, Chong RK, Kasama T, et al. Three-dimensional tomographic imaging and characterization of iron compounds within Alzheimer's plaque core material. *J Alzheimers Dis* 2008;14: 235-245.
11. Quintana C, Bellefqih S, Laval JY, et al. Study of the localization of iron, ferritin, and hemosiderin in Alzheimer's disease hippocampus by analytical microscopy at the subcellular level. *J Struct Biol* 2006;153:42-54.
12. Gerber MR, Connor JR. Do oligodendrocytes mediate iron regulation in the human brain? *Ann Neurol* 1989;26:95-98.
13. Connor JR, Menzies SL. Relationship of iron to oligodendrocytes and myelination. *Glia* 1996;17:83-93.
14. Hill JM, Switzer RC III. The regional distribution and cellular localization of iron in the rat brain. *Neuroscience* 1984;11:595-603.
15. Dhenain M, El Tannir El Tayara N, Wu TD, et al. Characterization of in vivo MRI detectable thalamic amyloid plaques from APP/PS1 mice. *Neurobiol Aging* 2007;30:41-53.
16. Vanhoutte G, Dewachter I, Borghgraef P, Van Leuven F, Van der Linden A. Noninvasive in vivo MRI detection of neuritic plaques associated with iron in APP[V717I] transgenic mice, a model for Alzheimer's disease. *Magn Reson Med* 2005;53:607-613.
17. Falangola MF, Ardekani BA, Lee SP, et al. Application of a nonlinear image registration algorithm to quantitative analysis of T2 relaxation time in transgenic mouse models of AD pathology. *J Neurosci Methods* 2005;144:91-97.
18. Galvez N, Fernandez B, Sanchez P, et al. Comparative structural and chemical studies of ferritin cores with gradual removal of their iron contents. *J Am Chem Soc* 2008;130(25):8062-8068.

19. Drayer B, Burger P, Darwin R, Riederer S, Herfkens R, Johnson GA. MRI of brain iron. *AJR Am J Roentgenol* 1986;147:103-110.
20. Gossuin Y, Hautot D, Muller RN, et al. Looking for biogenic magnetite in brain ferritin using NMR relaxometry. *NMR Biomed* 2005;18:469-472.
21. Gossuin Y, Roch A, Muller RN, Gillis P. Relaxation induced by ferritin and ferritin-like magnetic particles: the role of proton exchange. *Magn Reson Med* 2000;43:237-243.
22. Bulte JW, Vymazal J, Brooks RA, Pierpaoli C, Frank JA. Frequency dependence of MR relaxation times. II. Iron oxides. *J Magn Reson Imaging* 1993;3:641-648.
23. Vymazal J, Brooks RA, Baumgarner C, et al. The relation between brain iron and NMR relaxation times: an in vitro study. *Magn Reson Med* 1996;35:56-61.
24. Vymazal J, Zak O, Bulte JW, Aisen P, Brooks RA. T1 and T2 of ferritin solutions: effect of loading factor. *Magn Reson Med* 1996;36:61-65.
25. Haacke EM, Cheng NY, House MJ, et al. Imaging iron stores in the brain using magnetic resonance imaging. *Magn Reson Imaging* 2005;23:1-25.
26. Bizzi A, Brooks RA, Brunetti A, et al. Role of iron and ferritin in MR imaging of the brain: a study in primates at different field strengths. *Radiology* 1990;177:59-65.
27. Meguro R, Asano Y, Iwatsuki H, Shoumura K. Perfusion-Perls and -Turnbull methods supplemented by DAB intensification for non-heme iron histochemistry: demonstration of the superior sensitivity of the methods in the liver, spleen, and stomach of the rat. *Histochem Cell Biol* 2003;120:73-82.
28. Thomas LO, Boyko OB, Anthony DC, Burger PC. MR detection of brain iron. *AJNR Am J Neuroradiol* 1993;14:1043-1048.
29. Bussiere T, Bard F, Barbour R, et al. Morphological characterization of Thioflavin-S-positive amyloid plaques in transgenic Alzheimer mice and effect of passive A β immunotherapy on their clearance. *Am J Pathol* 2004;165:987-995.
30. Richardson JA, Burns DK. Mouse models of Alzheimer's disease: a quest for plaques and tangles. *ILAR J* 2002;43:89-99.
31. Duyckaerts C, Potier MC, Delatour B. Alzheimer disease models and human neuropathology: similarities and differences. *Acta Neuropathol* 2008;115:5-38.
32. van Groen T, Kiliaan AJ, Kadish I. Deposition of mouse amyloid beta in human APP/PS1 double and single AD model transgenic mice. *Neurobiol Dis* 2006;23:653-662.
33. Stopa B, Piekarska B, Konieczny L, et al. The structure and protein binding of amyloid-specific dye reagents. *Acta Biochim Pol* 2003;50:1213-1227.
34. Matsuoka Y, Picciano M, Malester B, et al. Inflammatory responses to amyloidosis in a transgenic mouse model of Alzheimer's disease. *Am J Pathol* 2001;158:1345-1354.
35. Gorevic PD, Castano EM, Sarma R, Frangione B. Ten to fourteen residue peptides of Alzheimer's disease protein are sufficient for amyloid fibril formation and its characteristic x-ray diffraction pattern. *Biochem Biophys Res Commun* 1987;147:854-862.
36. Luhrs T, Ritter C, Adrian M, et al. 3D structure of Alzheimer's amyloid-beta(1-42) fibrils. *Proc Natl Acad Sci U S A* 2005;102:17342-17347.
37. Yan Y, Liu J, McCallum SA, Yang D, Wang C. Methyl dynamics of the amyloid-beta peptides A β 40 and A β 42. *Biochem Biophys Res Commun* 2007;362:410-414.
38. Kim W, Hecht MH. Generic hydrophobic residues are sufficient to promote aggregation of the Alzheimer's A β 42 peptide. *Proc Natl Acad Sci U S A* 2006;103:15824-15829.
39. Fullerton GD, Potter JL, Dornbluth NC. NMR relaxation of protons in tissues and other macromolecular water solutions. *Magn Reson Imaging* 1982;1:209-226.
40. Fullerton GD, Finnie MF, Hunter KE, Ord VA, Cameron IL. The influence of macromolecular polymerization of spin-lattice relaxation of aqueous solutions. *Magn Reson Imaging* 1987;5:353-370.
41. Guntert A, Döbeli H, Böhrmann B. High sensitivity analysis of amyloid-beta peptide composition in amyloid deposits from human and PS2APP mouse brain. *Neuroscience* 2006;143:461-475.
42. Perry G, Cash AD, Smith MA. Alzheimer disease and oxidative stress. *J Biomed Biotechnol* 2002;2:120-123.
43. Smith MA. Oxidative stress and iron imbalance in Alzheimer disease: how rust became the fuss! *J Alzheimers Dis* 2006;9(Suppl):305-308.
44. Connor JR, Menzies SL. Cellular management of iron in the brain. *J Neurol Sci* 1995;134(Suppl):33-44.
45. Connor JR, Snyder BS, Beard JL, Fine RE, Mufson EJ. Regional distribution of iron and iron-regulatory proteins in the brain in aging and Alzheimer's disease. *J Neurosci Res* 1992;31:327-335.
46. Wegiel J, Wang KC, Imaki H, et al. The role of microglial cells and astrocytes in fibrillar plaque evolution in transgenic APP(SW) mice. *Neurobiol Aging* 2001;22:49-61.
47. Mehlhase J, Gieche J, Widmer R, Grune T. Ferritin levels in microglia depend upon activation: modulation by reactive oxygen species. *Biochim Biophys Acta* 2006;1763:854-859.
48. Miura T, Mitani S, Takanashi C, Mochizuki N. Copper selectively triggers beta-sheet assembly of an N-terminally truncated amyloid beta-peptide beginning with Glu3. *J Inorg Biochem* 2004;98:10-14.
49. Smith DG, Cappai R, Barnham KJ. The redox chemistry of the Alzheimer's disease amyloid beta peptide. *Biochim Biophys Acta* 2007;1768:1976-1990.
50. Ghribi O, Golovko MY, Larsen B, Schrag M, Murphy EJ. Deposition of iron and beta-amyloid plaques is associated with cortical cellular damage in rabbits fed with long-term cholesterol-enriched diets. *J Neurochem* 2006;99:438-449.
51. Rottkamp CA, Raina AK, Zhu X, et al. Redox-active iron mediates amyloid-beta toxicity. *Free Radic Biol Med* 2001;30:447-450.
52. Wengenack TM, Whelan S, Curran GL, Duff KE, Poduslo JF. Quantitative histological analysis of amyloid deposition in Alzheimer's double transgenic mouse brain. *Neuroscience* 2000;101:939-944.
53. Satou T, Cummings BJ, Head E, et al. The progression of beta-amyloid deposition in the frontal cortex of the aged canine. *Brain Res* 1997;774:35-43.
54. Hallgren B, Sourander P. The effect of age on the non-haem iron in the human brain. *J Neurochem* 1958;3:41-51.
55. Connor JR, Snyder BS, Arosio P, Loeffler DA, LeWitt P. A quantitative analysis of isoferritins in select regions of aged, parkinsonian, and Alzheimer's diseased brains. *J Neurochem* 1995;65:717-724.
56. Nakada T, Matsuzawa H, Igarashi H, Fujii Y, Kwee IL. In vivo visualization of senile-plaque-like pathology in Alzheimer's disease patients by MR microscopy on a 7T system. *J Neuroimaging* 2008;18:125-129.